Parasitic loss in microring-waveguide coupling and its impact on wideband nonlinear photonics

Yi Sun[1,2], **Daniel Pimbi**[1,2], **Xiyuan Lu**[1,2,4], **Jordan Stone**[1,2], **Junyeob Song**[1], **Zhimin Shi**[3], and **Kartik Srinivasan**[1,2,*]

[1] *Microsystems and Nanotechnology Division, Physical Measurement Laboratory, National Institute of Standards and Technology, Gaithersburg, MD 20899, USA*
[2] *Joint Quantum Institute, NIST/University of Maryland, College Park, MD 20742, USA*
[3] *Reality Labs Research, Meta, Redmond, WA 98052, USA*
[4] *Email: xiyuan.lu@nist.gov*
[*] *Corresponding author: kartik.srinivasan@nist.gov*

Compiled September 28, 2026

Microring resonators enable the enhancement of nonlinear frequency mixing processes, generating output fields at frequencies that widely differ from the inputs, in some cases by more than an octave. The efficiency of such devices depends on effective in- and out-coupling between access waveguides and the microrings at these widely separated frequencies. One successful approach is to separate the coupling task across multiple waveguides, with a cutoff waveguide (a waveguide that does not support guided modes above a certain wavelength) being judiciously used to prevent unwanted excessive overcoupling at low frequencies. Here, we examine how such a cutoff waveguide can still induce parasitic loss in the coupling region of a microring resonator, thereby impacting nonlinear device performance. We verified this parasitic loss channel through both experiment and simulation, showing that a waveguide optimized for 532 nm (visible) and 780 nm (near-infrared), while nominally cut off at 1550 nm, can still introduce significant parasitic loss at telecom wavelengths. This is studied in the context of visible-telecom optical parametric oscillation, where the excess parasitic loss can be strong enough to prevent threshold from being reached. Our finding elucidates a major challenge for wideband integrated nonlinear photonics processes when efficient coupling of widely-separated frequencies is needed.

http://dx.doi.org/10.1364/PRJ.XX.XXXXXX

1. INTRODUCTION

Nonlinear nanophotonics enables chip-integrated coherent light generation at frequencies outside of those available through conventional optical gain media, such as direct band gap gain in semiconductors. For high efficiency, such processes commonly rely on microresonators to enhance the effective strength of the nonlinear interaction [1–3]. Nonlinear conversion into the visible or within the visible is possible through a variety of second- and third-order nonlinear processes, such as Kerr microcomb generation [4–8], second- and third-harmonic generation (SHG and THG) [9–17], optical parametric oscillation (OPO) [18–23], stimulated four-wave mixing (StFWM) [24, 25], stimulated Brillouin scattering [26], and FWM-Bragg scattering (FWM-BS) [27]. The successful implementation of each of these nonlinear processes is based on management of microresonator nonlinearity, quality factor, dispersion, and waveguide coupling.

Microresonator-waveguide coupling is especially challenging when optimizing for multiple, widely-separated frequencies. Evanescent coupling depends on modal overlap, phase mismatch, and interaction length, and in general, the coupling rate increases as frequency decreases (wavelength increases), due to increased modal overlap. For microrings, point coupling, where the waveguide is tangent to the ring, can exhibit a coupling rate variation of a few orders-of-magnitude across an octave [28], as depicted in coupling scheme **i** in Fig. 1(a), with the geometry shown on top and a typical coupling quality factor (Q_c) spectrum shown on bottom. Thus, a waveguide designed to be critically coupled at short wavelengths results in strong overcoupling at long wavelengths. Pulley coupling [scheme **ii** in Fig. 1(a)], where the waveguide is wrapped around a portion of the ring, can reduce such coupling dispersion, though even optimized designs can exhibit more than one order of magnitude variation when bandwidths extend beyond an octave [28, 29]. To mitigate strong overcoupling in targeted spectral bands, the pulley coupling anti-resonances, in which local regions of the spectrum exhibit pronounced reduced coupling, can be carefully engineered, but is often highly sensitive to dimensional variations. On the other hand, unoptimized coupling strongly impacts the performance of wideband nonlinear nanophotonics

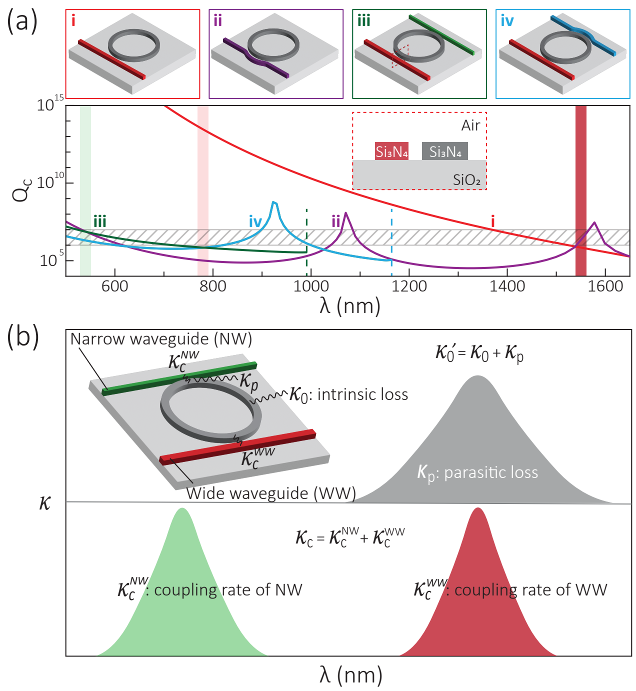

Fig. 1. **(a)** Four possible coupling schemes (top) for wideband, air-clad nonlinear integrated photonics that are designed to optimize coupling quality factor (Q_c) across visible (532 nm), near-infrared (780 nm), and telecom (1550 nm) wavelength bands highlighted in light green, pink and red, respectively (bottom). The inset shows a schematic of the coupling region between the waveguide (red) and the microring resonator (dark gray). The hatched gray rectangular area in the representative Q_c spectra denotes the design target for critical coupling with $Q_c = 10^6$ to 10^7. **i.** Single straight waveguide (red): critically coupled at 1550 nm, but severely undercoupled at shorter wavelengths; **ii.** Single pulley waveguide (purple): broadband coupling with a fabrication-sensitive pulley anti-resonance preventing overcoupling at 1550 nm. Despite this design effort, Q_c varies by two orders between the three targeted bands; **iii.** Two separate straight waveguides: one narrow, small-gap waveguide (green) is optimized for visible and near-infrared with a cutoff wavelength near 1000 nm, ensuring it only guides shorter wavelengths. The other wide, large-gap waveguide (red) is optimized for critical coupling at 1550 nm; **iv.** One straight waveguide combined with one pulley waveguide: similar to scheme **iii**, the straight waveguide (red) is designed for critical coupling at 1550 nm but now the narrow pulley waveguide (blue), with a cutoff wavelength near 1200 nm, has more optimal coupling at 532 nm and 780 nm. These two waveguides thus, in principle, cover all three bands optimally. **(b)** Detailed explanation of loss channels for scheme **iii** in **(a)**: the intrinsic loss (κ_0), dominated by material absorption and microring sidewall roughness scattering, exhibits weak wavelength dependence (varying within a factor of 3). For efficient coupling, the coupling rate (κ_c^{NW} and κ_c^{WW} for the narrow and wide waveguides, respectively) is typically designed to match κ_0, with slight under- or over-coupling depending on application needs. Here, we identify a parasitic loss channel (κ_p), induced by the narrow waveguide, which elevates the effective intrinsic loss ($\kappa_0' = \kappa_0 + \kappa_\mathrm{p}$) for longer wavelengths. Such loss is often overlooked but can have a strong impact on performance.

devices, for example, in term of conversion efficiency, output power, and other metrics.

A successful solution to this wideband coupling challenge is to take advantage of cutoff in waveguides with asymmetric cladding, which can be realized through a silicon dioxide (SiO_2) layer underneath the waveguide and air surrounding on all other sides, as shown in Fig. 1(a). For a given waveguide geometry, there exists a cutoff wavelength, above which guided modes are not supported [30]. This property doesn't exist for symmetrically clad rectangular waveguides, resulting in Q degradation at long wavelengths caused by parasitic loss, even when careful design is employed [17]. Using cutoff, the coupling task for wideband nonlinear photonics can be split between two (or more) waveguides, with each responsible for different spectral regions. Typically, a narrow width, small gap waveguide addresses shorter wavelengths (and is cutoff at long wavelengths), while a wider width, large gap waveguide addresses longer wavelengths (with negligible coupling at short wavelengths due to the large gap). Representative cases where the narrow width waveguide is point coupled [**iii** in Fig. 1(a)] or pulley coupled [**iv** in Fig. 1(a)] to the microring, and the wider width waveguide is point coupled to the microring in the same fashion as in **i** in Fig. 1(a), have been used for octave-spanning microcombs [31, 32], highly non-degenerate entangled photon pair sources [33], and telecom-to-visible spectral translation [24]. In addition to the coupling benefits, dispersion wise, the use of asymmetrically-clad structures naturally dovetails with visible wavelength dispersion engineering [6, 19], where a top air cladding eliminates the normal dispersion of the typical SiO_2 top cladding, which would otherwise require compensation in the resonator design.

A crucial assumption underlying the above strategy is that the cutoff waveguide has no impact on the resonator for sufficiently long wavelengths. However, in this paper, we report that this plausible assumption needs to be examined and executed with care: it turns out that even a waveguide satisfying the cutoff condition can still induce substantial parasitic loss (κ_p) in the microring, as depicted in Fig. 1(b), either due to scattering or coupling to leaky modes. We quantitatively study the impact of κ_p in the context of wideband Kerr OPO. Such OPOs enable the generation of visible light from a near-infrared pump [19, 20], with wavelengths across the full green gap spectral region recently been reported [23]. Our study highlights how the previously neglected κ_p contribution from a cutoff waveguide can limit extension of OPO spectral coverage deeper into the visible. In particular, we show that degradation of the Q of the long-wavelength idler mode inhibits OPO threshold from being reached, thereby setting a limit on the longest (and therefore shortest) wavelengths achievable in a given OPO design. Our results are vital in understanding how to design nonlinear nanophotonic devices to realize efficient conversion across the full range of wavelengths allowed by the resonator dispersion and material transparency.

2. RESULTS AND DISCUSSIONS

Out of various wideband nonlinear optical processes, we choose Kerr OPO as it is a highly informative tool to unveil the impact of the cutoff coupling waveguide on nonlinear light generation. The versatility of OPO lies in its ability to generate light across a wide range of signal and idler frequencies (ν_s and ν_i) by varying the pump frequency (ν_p), with a change of $\approx$ 5 THz enough to shift the output frequencies by $>$ 120 THz [19, 23]. Moreover, dispersion engineering by adjusting the ring width (RW) between devices on the same chip provides further tuning of the output frequencies [18–21, 23]. These characteristics enable a detailed analysis of the onset of performance degradation in terms of the widest OPO separation achievable at a given pump power, as the OPO threshold is inversely proportional to the Qs of all three modes involved [18]. This means that a sufficiently large reduction in Q as the targeted signal/idler bands become increasingly spectrally separated from the pump – for example, due to

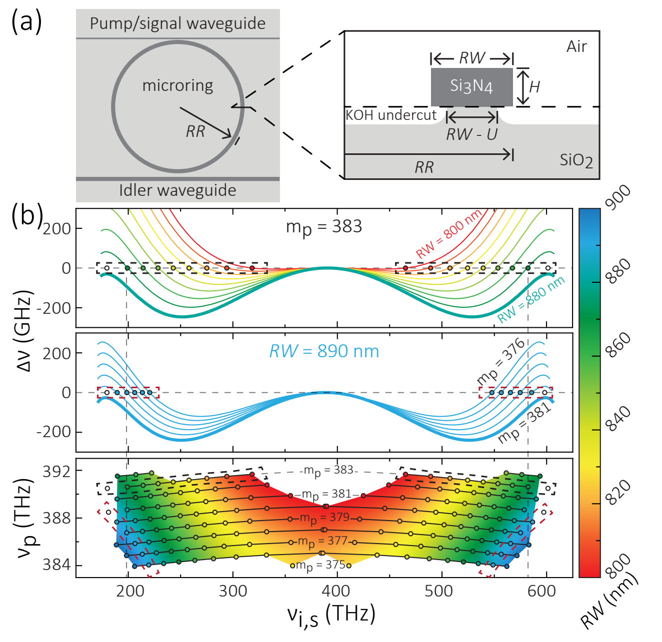

Fig. 2. **(a)** Schematic of a Kerr optical parametric oscillator (OPO) device with a zoomed-in cross-sectional view. The microring resonator features two waveguides for coupling the pump/signal and idler, respectively. The undercut structure is symmetrically etched using heated potassium hydroxide treatment. Key geometric parameters include the outer ring radius (*RR*), ring width (*RW*), Si_3N_4 thickness (*H*), and total undercut (*U*). **(b)** Simulated spectral coverage for OPO devices (*RR* = 25 µm, *H* = 600 nm, *U* = 140 nm, *RW* = 800 nm to 900 nm). Top panel: Frequency mismatch spectra ($\Delta\nu = \nu_s + \nu_i - 2\nu_p$) for *RW* = 800 nm to 880 nm with fixed $m_p = 383$. Middle panel: Spectra for *RW* = 890 nm with $m_p = 376$ to 381. Solid circles mark zero crossings, which predicted ν_s and ν_i frequencies with empty circles indicating configurations in which OPO is not supported. Bottom panel: Spectral map showing OPO coverage from ≈ 190 THz to ≈ 590 THz. Color scale denotes *RW* and odd m_p values are labeled. Dashed black and red boxes link to cases in the top and middle panels, respectively. Vertical dashed lines highlight degenerate ν_s/ν_i generation via multiple *RW* and m_p combinations.

excess parasitic loss induced by the cutoff waveguide at long wavelengths – would prevent threshold from being reached. In practice, it would be challenging to map *Q* and threshold at every wavelength due to laser availability and wavelength-dependent coupling; instead, we quantify performance by the maximum span at a fixed on-chip pump power. Such analysis would be challenging with other nonlinear processes like SHG and THG, which have no threshold power and generally lack the capacity to probe a broad set of output wavelengths within a single device. In addition, OPO, as an oscillation process seeded by vacuum fluctuations, is constrained by its threshold power, while the complementary process of StFWM, where a seed laser is injected along with the pump, is thresholdless. They can thus be used together to validate whether the inability to reach threshold is due to resonator dispersion or loss [24].

We utilize high-*Q* silicon nitride (Si_3N_4) microring resonators as a platform for our widely-separated OPO devices. The chip uses an underlying SiO_2 cladding and top side air cladding with all key parameters depicted in Fig. 2(a). Figure. 2(b) shows the simulated spectral coverage for such OPO devices with *RR* = 25 µm, *H* = 600 nm, *U* = 140 nm, and *RW* ranging from 800 nm to 900 nm. The undercut *U*, achieved by heated potassium hydroxide etching, helps to enhance the robustness of OPO generation [23]. The pump wavelength is constrained from 765 nm to 781 nm, matching the tuning range of the external cavity diode laser (ECDL) pump laser, corresponding to the pump mode azimuthal number (m_p) ranging from 375 to 384 for the fundamental transverse electric mode (TE_0) with the microring resonator geometries mention above. Simulations in Fig. 2(b) are performed through eigenmode calculations of the microrings using the finite-element method. For Kerr OPOs, a pair of ν_i and ν_s that are widely separated from ν_p can be achieved when the pump dispersion is normal but close to zero [18], and the frequency mismatch, defined as $\Delta\nu = \nu_s + \nu_i - 2\nu_p$, has a small but positive value ($\Delta\nu \gtrsim 0$). Two sets of frequency mismatch spectra are shown in the top and middle panels in Fig. 2(b). The top panel shows frequency mismatch spectra for nine devices with *RW* varying from 800 nm to 880 nm at a fixed $m_p = 383$, while the middle panel presents the spectra for a single device with *RW* = 890 nm while m_p ranges from 376 to 381. The solid circles are the zero-crossing points, which representing the prospective ν_i and ν_s for different *RW* and m_p combinations. The two bold curves don't have zero-crossing points, indicating that OPOs are not supported in those cases. m_p and *RW* thus serve as two tuning knobs for OPOs: When m_p is fixed at 383, as *RW* is increased from 800 nm to 870 nm, ν_i (ν_s) could cover the spectral range between ≈ 318 THz (≈ 465 THz) to ≈ 199 THz (≈ 582 THz); when *RW* is fixed at 890 nm, as m_p is increased from 376 to 381, ν_i (ν_s) could cover the spectral range between ≈ 219 THz (≈ 549 THz) to ≈ 189 THz (≈ 586 THz). The bottom panel in Fig. 2(b) shows the simulated spectral coverage of OPOs after exhausting all possible combinations of m_p and *RW*. In theory, these OPOs could generate any light between ≈ 190 THz to ≈ 590 THz.

In addition, the two vertical dashed lines connecting three panels in Fig. 2(b) demonstrate that several combinations of *RW* and m_p [parameterized as (*RW*, m_p)] can be employed to generate a specific ν_i or ν_s. For example, combinations of (870 nm, 383), (880 nm, 381), (890 nm, 379), and (900 nm, 377) could generate $\nu_i \approx 200$ THz, and other combinations of (870 nm, 383) and (900, 378) could generate $\nu_s \approx 582$ THz. This ability to reach the same ν_i or ν_s through multiple *RW* and m_p configurations provides a critical diagnostic capability: If a broader ν_i-ν_s span, as predicted by dispersion simulations, remains unattainable despite testing all viable *RW* and m_p combinations, the limitation must stem from a parameter outside those governing dispersion — specifically, as we will discuss later, the cutoff waveguide width.

In order to experimentally investigate the influence of κ_p on the idler due to the narrow coupling waveguide, we fabricate these OPO devices with dimensions as mentioned above while also varying the width of the pump/signal waveguide (W_p), thereby varying the wavelength at which long-wavelength cutoff occurs. The device design is created with the NIST Center for Nanoscale Science and Technology's Nanolithography Toolbox [34]. A silicon wafer is thermally oxidized to produce a 3 µm thick SiO_2 layer, followed by deposition of a 600 nm thick Si_3N_4 film using low-pressure chemical vapor deposition. Layer thicknesses and wavelength-dependent refractive indices are determined via spectroscopic ellipsometry and modeled with an extended Sellmeier equation. The wafer is then diced into small pieces for patterning. Electron beam lithography with positive tone resist defines the patterns, which are transferred to the Si_3N_4 via oxygen and fluoride-based reactive-ion etching. Post-etch chemical cleaning removes residual polymer, and the device is annealed at 1100 °C for 4 hours under nitrogen. An oxide lift-off process selectively air-clads the devices while preserving SiO_2 cladding on input/output waveguides for efficient

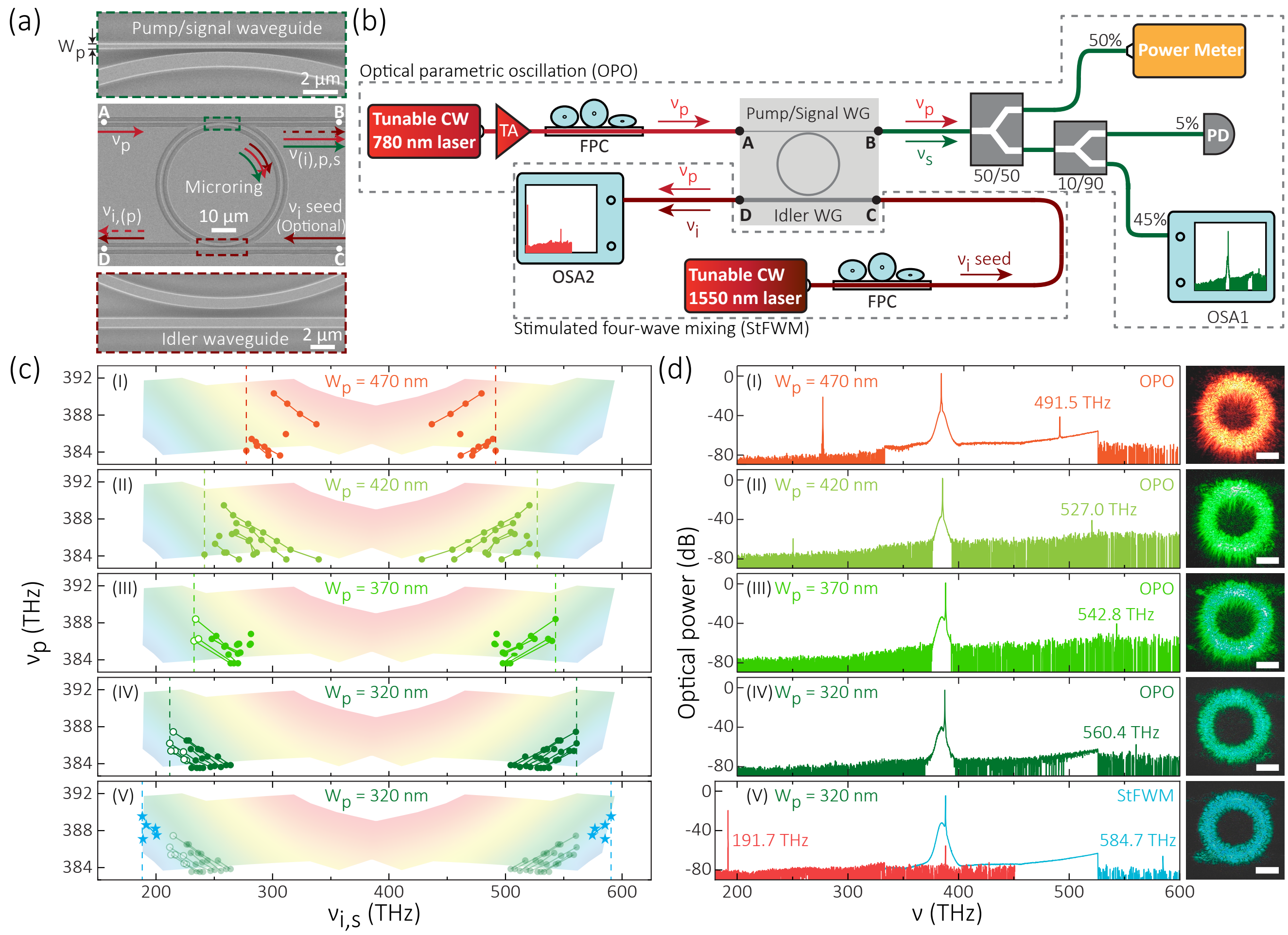

Fig. 3. **(a)** Scanning electron microscope (SEM) images of a Kerr OPO microring resonator, with zoomed-in views of pump/signal and idler coupling regions. The width of the pump/signal waveguide is defined as W_p. ν_p is injected through port A, with the residual pump and ν_s collected at port B. In cases where ν_i is cutoff through the pump/signal waveguide, it can be detected at port D together with residual pump. For stimulated four-wave mixing (StFWM), a seed at ν_i is injected at port C at the same time as the pump in port A. **b** Experimental setup for OPO and StFWM. TA: Tapered amplifier, FPC: Fiber polarization controller, OSA: Optical spectrum analyzer, PD: Photodiode. **(c)** Experimentally observed ν_s and ν_i for OPO (circles, I–V) and StFWM (stars, V) with different W_p. Solid circles: ν_s and ν_i directly obtained from OSA1; empty circles: ν_i calculated via energy conservation from measured ν_p and ν_s. Stars: ν_s measured at OSA1 and ν_i measured at OSA2. Simulated spectral coverage from Fig. 2(b) (shadowed in the background for comparison) closely matches experimental data, using identical geometries. Vertical dashed lines mark maximum $\nu_i - \nu_s$ spans for each W_p. **(d)** Widest OPO (I – IV) and StFWM (V) spectra in **(c)**. Here, 0 dB is referenced to 1 mW, i.e., dBm. Idler cutoff through the pump/signal waveguide occurs in III, IV, and V collecting no idler in OSA1, while spectrum in V combines the spectra recorded from OSA1 and OSA2. The right panel shows the optical microscope images of scattered signal light with 20 µm scale bars.

edge coupling. Microring undercuts are formed via 70 °C KOH etching, with lateral etching rates calculated from vertical rate measurements and validated by cross-sectional scanning electron microscope (SEM) imaging. The chip is diced, polished, and prepared for lensed-fiber coupling.

Figure 3(a) shows the SEM images of the fabricated devices. Two straight waveguides are used to inject and extract light in and out of the OPOs, following scheme **iii** from Fig. 1(a). The narrow waveguide, of width W_p and with a small coupling gap, is designed to in-couple the pump through port A and out-couple the pump and signal light through port B, and is cut-off in the idler band. The second (wide) waveguide with a large coupling gap is designed to out-couple the idler light at long wavelengths through port D. The zoomed-in SEM images show the coupling regions for these two waveguides. The measurement setup is shown in Figure 3(b). An amplified ECDL with tunable range between 765 nm to 781 nm is injected from port A through lensed fiber after fiber polarization controller. The on-chip pump power is limited ≈ 100 mW with a calibrated insertion loss ≈ 3 dB per facet for the pump. The device *RW* and pump mode selected act as two tuning parameters, as illustrated previously in Figure 2(b). OPO can be observed in devices with appropriate *RW* configurations when the on-chip pump power exceeds the threshold while the pump wavelength is scanned from shorter to longer wavelengths, provided dispersion conditions are properly engineered. When OPO is generated, ν_s, ν_p, and ν_i (when shorter than the cutoff wavelength for the pump/signal waveguide) can be recorded from OSA1 through port B. OSA2 through port D can be used to record ν_i and part of ν_p as the wider idler waveguide is designed for critically coupling ν_i but undercoupling for ν_p and ν_s. Another tunable laser at telecom wavelengths near ν_i can be injected from port C (the wide waveguide input) in addition to ν_p injection at port A for StFWM experiments, which can be used to validate the dispersion.

Figure 3(c)[(I) - (IV)] show the experimentally observed OPO ν_i and ν_s distributions for different W_p values. Data points within the same connected line are from a single device with the same *RW*. Simulated spectral coverage in the bottom panel of Fig. 2(b) is shadowed in the background, and shows a good consistency between the simulation and experiment. Figure 3(d)[(I) - (IV)] display the widest achievable OPO spectrum for different W_p, with the right panel showing representative optical microscope images of scattered light of the generated visible signal. This plot clearly shows that, for a given W_p, there is a ν_i-ν_s span limit (marked with dashed lines), with multiple OPO devices with different *RW* reaching this maximum OPO span at different ν_p. The widest ν_i-ν_s span increases from ≈ 210 THz to ≈ 350 THz as W_p decreases from 470 nm to 320 nm, as demonstrated from (I) to (IV). Clearly, W_p significantly impacts the maximum OPO span, even if the resonator dispersion and pump mode suggest that wider OPO is achievable.

To that end, we perform StFWM experiments to confirm that our OPO span is not limited by an inability to achieve phase- and frequency-matching. For the same devices with W_p = 320 nm, when injecting a seed laser near ν_i from port C in addition to the near-infrared pump from port A, we are able to see extended ν_i-ν_s spans up to ≈ 390 THz, thereby achieving the edge of the simulated spectral coverage, as shown in Fig. 3(c)(V). Figure 3(d)(V) displays a typical StFWM spectrum created by combining the spectra recorded from OSA1 and OSA2, while the right panel shows the generated representative cyan color scattered from the microring. Compared to OPO, StFWM is a significantly more efficient process with no threshold power requirement [24]. This extension of the ν_i-ν_s span for the same set of devices under StFWM demonstrates that the resonator dispersion is not likely to be the limitation on the OPO span in (IV), and suggests that *Q* degradation may instead be the cause.

To investigate the reason for OPO performance degradation with increasing W_p, we measure the intrinsic quality factor (Q_0) near 1600 nm using the idler waveguide as shown in Fig. 4(a). These devices feature the same geometric parameters including the *RR* of 25 μm, *H* of 600 nm, and *RW* of 850 nm, with the only variation being in W_p, which ranges from 235 nm to 495 nm. This narrow pump/signal waveguide is designed to remain below cutoff for all W_p in the telecom band, so 1600 nm provides a consistent operating point for Q extraction and field visualization. Figure 4(b) shows SEM images for the coupling regions, transmission measurements, and the fits to extract Q_0 at 1600 nm when W_p = 270 nm, 370 nm, and 470 nm. We find that Q_0 decreases from ≈ 2.5×10^5 to ≈ 2.7×10^4 as W_p increases from 270 nm to 470 nm. Figure 4(c) summarizes the Q_0 trends with different W_p values under three different coupling gap configurations, and clearly show a substantial decrease of Q_0 with increasing W_p in all cases. This significant reduction in Q_0 for a prospective idler mode elevates its OPO threshold [19]. Functionally, this means that for a given W_p, there is a maximum idler wavelength (and hence minimum signal wavelength) for which OPO threshold is reached given the pump power available. This is consistent with the experimental observations in Fig. 3, where larger W_p limits the shortest achievable OPO signal wavelength and longest OPO idler wavelength.

Conventionally, Q_0 in microring resonators is only determined by material absorption and sidewall scattering losses. However, the devices studied here — created in a single fabrication run on the same piece (less than 4 cm^2 area) and with identical microring geometries (*RR*, *H*, and *RW*) — exhibit an order-of-magnitude variation in Q_0 at the idler band [Fig. 4(c)]. This discrepancy cannot be attributed to fabrication nonuniformity, as the process-induced variations in material and scattering losses are negligible within 4 cm^2 area. The sole distinguishing parameter is the pump/signal waveguide width W_p, which is intentionally varied below the cutoff width for telecom wavelengths. Thus, contrary to initial expectations, where such sub-cutoff W_p was assumed to negligibly perturb long-wavelength modes (e.g., idler wavelengths $\lambda_i \approx 1600$ nm), the observed Q_0 degradation implies an unaccounted κ_p arising from the cutoff waveguide, as illustrated in Fig. 1(b).

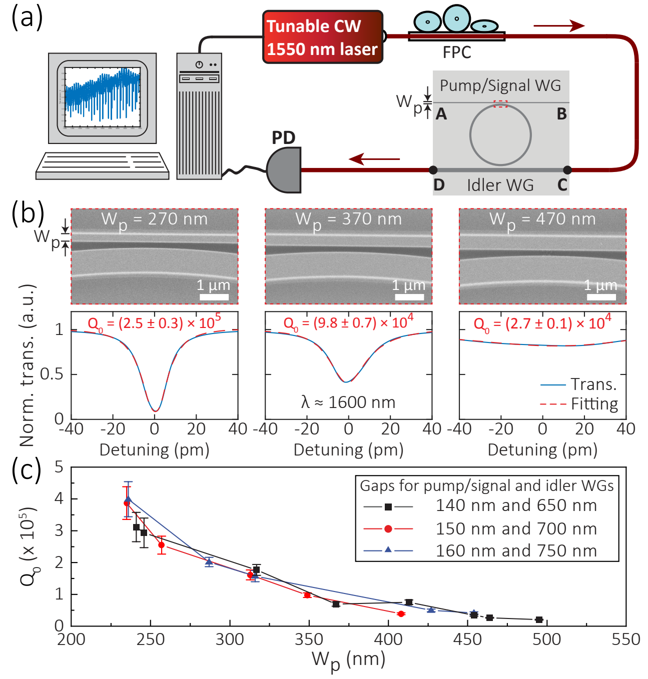

Fig. 4. **(a)** Setup for telecom wavelength transmission measurements through the idler waveguide and in the presence of a varying width pump/signal waveguide. **(b)** Top-view SEM images for the pump/signal waveguide coupling region with red dashed box in **a** for W_p = 270 nm, 370 nm, and 470 nm. The bottom panels show corresponding Q measurements and fits near 1600 nm for these W_p values. **(c)** Summary of the intrinsic quality factor (Q_0) for modes near 1600 nm as a function of W_p with three different coupling gap configurations, which clearly shows that Q_0 at the telecom wavelength is significantly degraded as W_p increases. The uncertainties in **(b)** and error bars in **(c)** are one standard deviation values from the fits.

We further validate our experimental observation of the reduction in Q_0 with increasing W_p through 3D finite-difference time-domain (FDTD) simulations. We analyze κ_p by focusing on the coupling region of the ring and pump/signal waveguide through the simulation configurations illustrated in Fig. 5(a). Detailed simulation setup and methodology is provided in the appendix below. Figure 5(b) illustrates the 3D FDTD simulation results for the pump/signal waveguide coupling region at λ = 1600 nm for W_p of 350 nm, 550 nm, and 700 nm. The top- and cross-sectional- views [field 1 and field 2 in Fig. 5(a)] of simulation results are displayed in the left and right panels, respectively. For W_p = 350 nm [top panel of Fig. 5(b)], the waveguide width lies far below the cutoff, resulting in no observable light coupling into the pump/signal waveguide, and the microring remains unaffected, with nearly all power retained in the through port. As W_p increases to 550 nm [middle panel of Fig. 5(b)], partial coupling occurs despite the width remaining below the cutoff threshold. Here, light coupled into the pump/signal waveguide radiates and leaks into the substrate

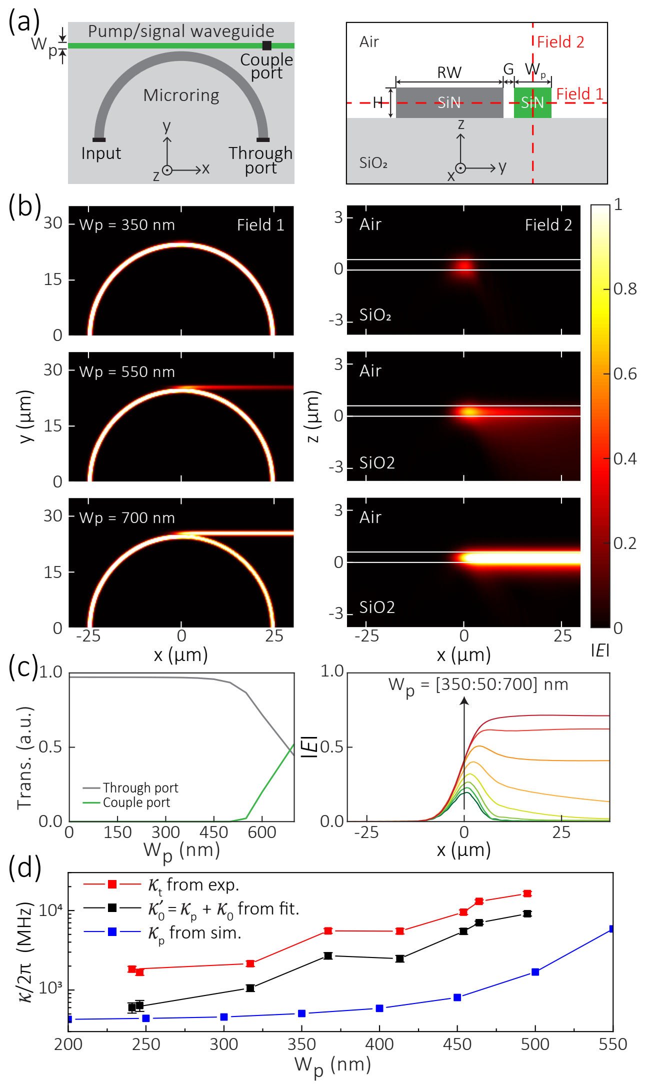

Fig. 5. **(a)** Schematics of 3D finite-difference time-domain (3D FDTD) simulation configurations from top (left panel) and cross-sectional (right panel) views. **(b)** Simulated normalized electric field profiles in the microring-pump/signal waveguide coupling region for W_p = 350, 550, and 700 nm. Left panels show top-view profiles at the plane marked by the red dashed line for field 1, and right panels show cross-sectional profiles along the pump/signal waveguide midplane for field 2, as defined in the right panel of **(a)**. **(c)** Left panel shows the transmission at the through port and couple port as the function of W_p. Right panel shows the cut-field lines through the pump/signal waveguide showing the electric field decay lengths. **(d)** Comparison of κ_p extracted from 3D FDTD simulation with the combination of κ_p and κ_0 extracted from experiments in Fig. 4.

along the propagation direction. Although such light is unlikely to reach the chip facet (where it could be measured), it nevertheless results in significant κ_p. Finally, at W_p = 700 nm [bottom panel of Fig. 5(b)], which is close to the cutoff width, efficient coupling is achieved with minimal radiative and leakage losses to the substrate, enabling stable light propagation along the waveguide.

These observations are quantified in Fig. 5(c). The left panel shows transmission at the through and coupled ports as a function of W_p, while the right panel illustrates intensity decay along the pump/signal waveguide. The results clearly suggest three regimes for W_p in the pump/signal waveguide. Firstly, at considerably smaller W_p than the nominal cutoff value (i.e., W_p = 350 nm), the pump/signal waveguide has little impact on telecom propagation within the ring, resulting in approximately zero power being coupled from the microring to it. Second, in the intermediate regime, near but still below the nominal cutoff value (W_p ranging from 500 nm to 600 nm), the microring couples telecom light to the pump/signal waveguide, with that coupled light strongly radiating into the substrate as it propagates away from the ring. This light coupled into the pump/signal waveguide results in non-zero κ_p for the telecom (idler) mode. Third, at sufficiently large W_p with respect to the cutoff value (W_p = 700 nm), the microring couples to a propagating waveguide mode with negligible radiative and leakage losses, as typical in a standard resonator-waveguide coupler.

Parasitic loss induced by the pump/signal waveguide thus depends critically on its width relative to the 700 nm cutoff for λ = 1600 nm. While conventional designs assume κ_p is negligible for sub-cutoff waveguide widths, our results demonstrate that even in an intermediate regime where W_p is significantly below cutoff e.g., (at 550 nm) — where the waveguide cannot guide light over long distances — partial coupling from the microring persists, creating a significant κ_p. This coupling to a leaky waveguide mode, visible in the radiative and substrate leakage at W_p = 550 nm [middle panel of Fig. 5(b)], highlights the key oversight in assuming sub-cutoff widths universally suppress κ_p. To eliminate κ_p entirely, W_p must be well below the intermediate regime (e.g., 350 nm in this case), as evidenced by the near-zero intensity decay in the top panel of Fig. 5(b). Here, the intermediate regime refers to the near-cutoff window where the pump/signal waveguide, though nominally below cutoff, couples light into short-propagation-length leaky substrate modes rather than supporting a fully guided mode, thereby adding a parasitic loss channel. The onset of this regime is wavelength dependent and is set by modal confinement, including core dimensions, the coupling gap, and the core–cladding index contrast. Thus, avoiding the intermediate regime is essential for applications targeting the widest OPO ν_i-ν_s span.

Figure 5(d) compares the experimentally extracted and simulated κ_p as a function of W_p. The total loss κ_t (red curve) comprises the microring's intrinsic loss κ_0, the parasitic coupling loss κ_p to the pump/signal waveguide, and the coupling loss to the idler waveguide. The black curve represents the effective intrinsic loss $\kappa_0' = \kappa_0 + \kappa_p$, derived from quality factor fits [consistent with Fig. 4(c)]. The blue curve corresponds to κ_p obtained from 3D FDTD simulations,which capture waveguide-mediated leakage to substrate modes but do not include scattering from the coupling waveguide and gap region. Despite systematic offsets attributed to unmodeled material absorption and scattering losses in the experiment, both datasets exhibit a monotonic increase in κ_p with W_p, validating the intermediate regime's role in parasitic coupling. The remaining discrepancy in onset and magnitude likely arises because the experimental κ_p aggregates both waveguide-mediated leakage and scattering introduced by the presence of the coupling waveguide, whereas the simulation includes only the leakage loss channel. Isolating and quantifying the waveguide-scattering contribution is left for future work.

3. CONCLUSION

In this work, we identify and quantify a critical parasitic loss channel in microring resonators arising from cutoff waveguides, a phenomenon previously overlooked in wideband nonlinear photonic designs. While conventional approaches assume that sub-cutoff waveguides negligibly perturb resonator modes, our experiments and simulations reveal a significant intermediate regime where coupling persists, albeit to a waveguide mode that is leaky and has a very short propagation length. In this regime, light partially couples from the microring into the nominally cutoff pump/signal waveguide, radiating into the substrate and introducing κ_p that degrades the intrinsic quality factor of idler modes at long wavelengths by up to an order of magnitude. This effect directly impacts nonlinear processes such as OPO, where elevated losses at the idler wavelength can prevent the system from reaching threshold, thereby limiting spectral coverage. We confirm this behavior in experiments that conclusively demonstrate OPO spans that are dependent on the width of this cutoff waveguide, with stimulated four-wave mixing experiments verifying that phase- and frequency-matching are not the limitation on achievable OPO spans.

Our 3D FDTD simulations elucidate the underlying mechanism: even waveguide widths slightly below the formal cutoff support evanescent coupling sufficient to extract light from the microring, yet insufficient to guide light efficiently, still resulting in radiative leakage. Crucially, κ_p are suppressed only when waveguide widths are designed well below the intermediate regime, as evidenced by the near-zero field decay in such configurations. These findings suggest a revised design guideline for wideband microring devices using air-cladding configures, emphasizing that cutoff compliance alone is inadequate for minimizing κ_p. Instead, rigorous avoidance of the intermediate regime is essential to ensure robust pump/signal and idler isolation and to enable nonlinear processes requiring high Q across widely separated spectral bands, such as visible-telecom OPO. Moreover, these design principles are equally critical for other wideband nonlinear photonics processes — like Kerr microcomb generation, SHG, THG, StFWM and FWM-BS — where maintaining high Q at key operative wavelengths is vital for optimal performance. This insight advances the engineering of integrated photonic platforms for applications demanding octave-spanning spectral control.

Appendix: Simulation Method The geometric parameters in the simulation for the microrings are the same as in the previous experiment with $RR = 25$ μm, RW = 850 nm, and H = 600 nm. W_p is our sweep parameter, ranging from 200 nm to 700 nm with a step size of 50 nm, while the gap is fixed at 140 nm. Our simulation setup incorporates three ports: an input port (from the microring) as the mode source, a through port with a mode expansion monitor after the coupling region, and a couple port with a mode expansion monitor at the pump/signal waveguide output. Additionally, two field monitors are positioned strategically – one in the top view plane at half the waveguide thickness (field 1) and the other in the middle along the length of the pump/signal waveguide (field 2), as shown in Fig. 5(a). The entire simulation is enclosed within a region bounded by perfectly matched layers, utilizing a Cartesian mesh grid of 20 nm. We launch a fundamental TE_0 mode at the input port, which propagates in the ring to the through port, with a portion of the power being coupled to the pump/signal waveguide.

To evaluate κ_p in simulations, we utilize the mode expansion monitors and extract the scattering matrices data containing the transmission coefficients. This data is then used to compute the normalized transmission modal powers at both the through and couple ports, as shown in Fig. 5(a). However, recording all the power coupled to the pump/signal waveguide at the location of the couple port is challenging due to power radiation and leakage to the substrate caused by the cutoff pump/signal waveguide mode regime. Instead, we calculated the power coupled to the pump/signal waveguide by subtracting the transmitted through power from the input power. Notably, at $W_p = 0$ (in the absence of the pump/signal waveguide), we observed that the microring resonator itself introduces additional bending and scattering losses. Thus, to ensure the reliability of our results, we conducted thorough convergence testing. Specifically, regarding the Cartesian mesh grid, we observed little impact on the results (i.e., the transmission spectrum does not uniformly vary with the increase in the mesh grid size). We attribute the resonator's intrinsic loss to bending and scattering losses from the microring resonator itself, along with a small contribution of loss/uncertainty due to the Cartesian mesh grid. Finally, we numerically determined κ_p by subtracting the transmitted through power and the resonator's intrinsic loss from the input power.

Data Availability The data that supports the plots within this paper and other findings of this study are available from the corresponding author upon reasonable request.

Acknowledgements This work is supported by the DARPA LUMOS and NIST-on-a-chip programs. The authors acknowledge Eric Stanton and Ashutosh Rao for helpful discussions.

Author Contributions X.L., Y.S., and J.S. carried out the design and simulation of the OPO devices. X.L. and Y.S. carried out the fabrication. Y.S. and J.S. carried out the measurements. D.P. carried out the simulation of parasitic coupling loss. All authors participated in analysis and discussion of results. Y.S. and K.S. wrote the manuscript with the help from others and K.S. supervised the project.

Competing Financial Interests The authors declare no competing financial interests.

REFERENCES

1. T. J. Kippenberg, A. L. Gaeta, M. Lipson, and M. L. Gorodetsky, "Dissipative Kerr solitons in optical microresonators," Science **361**, eaan8083 (2018).
2. J. K. S. Poon, A. Govdeli, A. Sharma, X. Mu, F.-D. Chen, T. Xue, and T. Liu, "Silicon photonics for the visible and near-infrared spectrum," Adv. Opt. Photonics **16**, 1–59 (2024).
3. X. Lu, L. Chang, M. A. Tran, T. Komljenovic, J. E. Bowers, and K. Srinivasan, "Emerging integrated laser technologies in the visible and short near-infrared regimes," Nat. Photonics **18**, 1010–1023 (2024).
4. E. Obrzud, V. Brasch, T. Voumard, A. Stroganov, M. Geiselmann, F. Wildi, F. Pepe, S. Lecomte, and T. Herr, "Visible blue-to-red 10 ghz frequency comb via on-chip triple-sum-frequency generation," Opt. Lett. **44**, 5290–5293 (2019).
5. Y. Zhao, X. Ji, B. Y. Kim, P. S. Donvalkar, J. K. Jang, C. Joshi, M. Yu, C. Joshi, R. R. Domeneguetti, F. A. S. Barbosa, P. Nussenzveig, Y. Okawachi, M. Lipson, and A. L. Gaeta, "Visible nonlinear photonics via high-order-mode dispersion engineering," Optica. **7**, 135–141 (2020).
6. G. Moille, D. Westly, R. Shrestha, K. T. Hoang, and K. Srinivasan, "Broadband visible wavelength microcomb generation in silicon nitride microrings through air-clad dispersion engineering," Laser & Photonics Rev. **19**, 2401746 (2025).
7. M. Corato-Zanarella, X. Ji, A. L. Gaeta, and M. Lipson, "Simultaneous on-chip generation of violet, blue, cyan, green, yellow, orange, and red light from an octave-spanning infrared frequency comb," Opt. Express **33**, 14581–14590 (2025).
8. Y. Li, Y. Yao, G. Li, X. Zhu, X. Wang, R. R. Davidson, B. E. Little, J. He, S. T. Chu, and Z. Kang, "Visible phase-locked microcombs generation in high-index doped silica glass micro-ring resonators," Laser & Photonics Rev. **19**, 2401688 (2025).

9. T. Carmon and K. J. Vahala, “Visible continuous emission from a silica microphotonic device by third-harmonic generation,” Nat. Phys. **3**, 430–435 (2007).
10. J. Lin, Y. Xu, J. Ni, M. Wang, Z. Fang, L. Qiao, W. Fang, and Y. Cheng, “Phase-matched second-harmonic generation in an on-chip $\mathrm{LiNbO_3}$ microresonator,” Phys. Rev. Appl. **6**, 014002 (2016).
11. J. B. Surya, X. Guo, C.-L. Zou, and H. X. Tang, “Efficient third-harmonic generation in composite aluminum nitride/silicon nitride microrings,” Optica. **5**, 103–108 (2018).
12. J. B. Surya, X. Guo, C.-L. Zou, and H. X. Tang, “Control of second-harmonic generation in doubly resonant aluminum nitride microrings to address a rubidium two-photon clock transition,” Opt. Lett. **43**, 2696–2699 (2018).
13. L. Chang, A. Boes, P. Pintus, J. D. Peters, M. J. Kennedy, X.-W. Guo, N. Volet, S. Yu, S. B. Papp, and J. E. Bowers, “High efficiency SHG in heterogenous integrated GaAs ring resonators,” APL Photonics **4**, 036103 (2019).
14. X. Lu, G. Moille, A. Rao, D. A. Westly, and K. Srinivasan, “Efficient photoinduced second-harmonic generation in silicon nitride photonics,” Nat. Photonics **15**, 131–136 (2020).
15. J. Hu, E. Nitiss, J. He, J. Liu, O. Yakar, W. Weng, T. J. Kippenberg, and C.-S. Brès, “Photo-induced cascaded harmonic and comb generation in silicon nitride microresonators,” Sci. Adv. **8**, eadd8252 (2022).
16. E. Nitiss, B. Zabelich, J. Hu, A. Stroganov, and C.-S. Brés, “Tunable photo-induced second-harmonic generation in a mode-engineered silicon nitride microresonator,” Opt. Express **31**, 14442–14453 (2023).
17. B. Li, Z. Yuan, W. Jin, L. Wu, J. Guo, Q.-X. Ji, A. Feshali, M. Paniccia, J. E. Bowers, and K. J. Vahala, “High-coherence hybrid-integrated 780 nm source by self-injection-locked second-harmonic generation in a high-q silicon-nitride resonator,” Optica **10**, 1241–1244 (2023).
18. X. Lu, G. Moille, A. Singh, Q. Li, D. A. Westly, A. Rao, S.-P. Yu, T. C. Briles, S. B. Papp, and K. Srinivasan, “Milliwatt-threshold visible-telecom optical parametric oscillation using silicon nanophotonics,” Optica **6**, 1535–1541 (2019).
19. X. Lu, G. Moille, A. Rao, D. A. Westly, and K. Srinivasan, “On-chip optical parametric oscillation into the visible: generating red, orange, yellow, and green from a near-infrared pump,” Optica **7**, 1417–1425 (2020).
20. R. R. Domeneguetti, Y. Zhao, X. Ji, M. Martinelli, M. Lipson, A. L. Gaeta, and P. Nussenzveig, “Parametric sideband generation in cmos-compatible oscillators from visible to telecom wavelengths,” Optica **8**, 316–322 (2021).
21. J. R. Stone, X. Lu, G. Moille, and K. Srinivasan, “Efficient chip-based optical parametric oscillators from 590 to 1150 nm,” APL Photonics **7**, 121301 (2022).
22. V. Ng, F. Azeem, L. S. Trainor, H. G. L. Schwefel, S. Coen, M. Erkintalo, and S. G. Murdoch, “Wideband multimode optical parametric oscillation in a kerr microresonator,” Opt. Express **31**, 5475–5482 (2023).
23. Y. Sun, J. Stone, X. Lu, F. Zhou, J. Song, Z. Shi, and K. Srinivasan, “Advancing on-chip Kerr optical parametric oscillation towards coherent applications covering the green gap,” Light. Sci. Appl. **13**, 201 (2024).
24. X. Lu, G. Moille, Q. Li, D. A. Westly, A. Rao, S.-P. Yu, T. C. Briles, S. B. Papp, and K. Srinivasan, “Efficient telecom-to-visible spectral translation using silicon nanophotonics,” Nat. Photonics **13**, 593–601 (2019).
25. S. Ramelow, A. Farsi, Z. Vernon, S. Clemmen, X. Ji, J. E. Sipe, M. Liscidini, M. Lipson, and A. L. Gaeta, “Strong nonlinear coupling in a $\mathrm{si_3n_4}$ ring resonator,” Phys. Rev. Lett. **122**, 153906 (2019).
26. N. Chauhan, A. Isichenko, K. Liu, J. Wang, Q. Zhao, R. O. Behunin, P. T. Rakich, A. M. Jayich, C. Fertig, C. W. Hoyt, and D. J. Blumenthal, “Visible light photonic integrated brillouin laser,” Nat. Commun. **12**, 4685 (2021).
27. Q. Li, M. Davanço, and K. Srinivasan, “Efficient and low-noise single-photon-level frequency conversion interfaces using silicon nanophotonics,” Nat. Photonics **10**, 406–414 (2016).
28. G. Moille, Q. Li, T. C. Briles, S.-P. Yu, T. Drake, X. Lu, A. Rao, D. Westly, S. B. Papp, and K. Srinivasan, “Broadband resonator-waveguide coupling for efficient extraction of octave-spanning microcombs,” Opt. Lett. **44**, 4737–4740 (2019).
29. G. Moille, E. F. Perez, J. R. Stone, A. Rao, X. Lu, T. S. Rahman, Y. K. Chembo, and K. Srinivasan, “Ultra-broadband kerr microcomb through soliton spectral translation,” Nat. Commun. **12**, 7275 (2021).
30. A. Yariv and P. Yeh, *Photonics: optical electronics in modern communications*, The Oxford series in electrical and computer engineering (Oxford University Press, New York, 2007), 6th ed.
31. Q. Li, T. C. Briles, D. A. Westly, J. R. Stone, B. R. Ilic, S. A. Diddams, S. B. Papp, and K. Srinivasan, “Octave-spanning microcavity Kerr frequency combs with harmonic dispersive-wave emission on a silicon chip,” in *Frontiers in Optics 2015,* (OSA, San Jose, California, 2015), p. FW6C.5.
32. T. C. Briles, J. R. Stone, T. E. Drake, D. T. Spencer, C. Fredrick, Q. Li, D. Westly, B. R. Ilic, K. Srinivasan, S. A. Diddams, and S. B. Papp, “Interlocking Kerr-microresonator frequency combs for microwave to optical synthesis,” Opt. Lett. **43**, 2933–2936 (2018).
33. X. Lu, Q. Li, D. A. Westly, G. Moille, A. Singh, V. Anant, and K. Srinivasan, “Chip-integrated visible-telecom photon pair sources for quantum communication,” Nat. Phys. **15**, 373–381 (2019).
34. K. C. Balram, D. A. Westly, M. I. Davanco, K. E. Grutter, Q. Li, T. Michels, C. H. Ray, R. J. Kasica, C. B. Wallin, I. J. Gilbert, B. A. Bryce, G. Simelgor, J. Topolancik, N. Lobontiu, Y. Liu, P. Neuzil, V. Svatos, K. A. Dill, N. A. Bertrand, M. Metzler, G. Lopez, D. Czaplewski, L. Ocola, K. A. Srinivasan, S. M. Stavis, V. A. Aksyuk, J. A. Liddle, S. Krylov, and B. R. Ilic, “The nanolithography toolbox,” J. Res. Natl. Inst. Stand. Technol. **121**, 464–475 (2016).